40 K, high-resolution measurements with an energy resolution of several meV are required. The larger value of α (0.46–0.48) strongly indicates that the long-range Coulomb interaction plays an important role in SWNTs. □

Methods

Sample preparation

In photoemission measurements, a relatively large sampling area is generally needed to obtain reliable data. According to theoretical band structure calculations[18], the electronic structure shows drastic changes depending on the diameter and helical arrangement of the SWNTs. It is very important to prepare a large sample consisting of SWNTs with uniform diameters. At present, however, no methods have been found that make diameters completely uniform. In this study, the SWNT samples were prepared by the laser vaporization method, in which the diameters of SWNTs can be controlled to some extent by the temperature of the furnace[22]. The SWNT-A (A1and A2) and SWNT-B samples in this work were prepared using a NiCo catalyst at 1,200 °C and 1,050 °C, respectively, in the furnace. The raw soot containing SWNTs was heated to 650 °C in a dynamic vacuum to remove the fullerenes, and then refluxed in 15% H_2O_2/water solution at 100 °C for 3 h. In the reflux process, active oxygen can burn out amorphous-carbon particles at 100 °C. After washing out the brownish by-products by careful filtration, the purified SWNTs were formed into thin black paper. Finally, the remaining metal particles were vaporized in a high vacuum at 1,250 °C. The obtained 'bucky paper' had a thickness of about 0.03 mm. The lengths of the SWNTs were several micrometres. The purity of the SWNT samples was estimated by electron-energy-loss spectroscopy to be higher than 90% (ref. 30). The mean diameters of the SWNTs in the SWNT-A and SWNT-B samples were estimated to be 1.37 nm and 1.25 nm, respectively, from the A_{1g} breathing mode frequencies in the Raman spectra. The resistivity of ~18 mΩ cm at 300 K increased with decreasing temperature, and amounted to ~65 mΩ cm at 8 K. The temperature dependence was consistent with the results of ref. 31.

Measurements

The photoemission spectra were measured using a SIENTA SES200 analyser at beamlines BL-11D of the Photon Factory, High Energy Accelerator Research Organization (KEK-PF) and BL-1 of the Hiroshima Synchrotron Radiation Center (HiSOR), Hiroshima University. The total energy resolution was set to 50 meV at KEK-PF, and 13 meV or 15 meV at HiSOR. The SWNT samples were placed on a Cu substrate, because the photoemission spectra were similar as a whole to those measured using an Au substrate. The SWNT samples were cooled to 10 K. The surfaces of the samples were cleaned by heating them up to 220 °C in an ultrahigh vacuum of about 2×10^{-10} torr. The cleanliness of the sample surface was checked by the signal from the O 2*p* level. The zero of the binding energy was calibrated for the Fermi edge of the evaporated Au thin film. The optical absorption spectrum was measured using a HITACHI U-3500 spectrophotometer for thin films of SWNTs prepared by a splay method on a glass substrate[23]. The Raman spectra were measured using a 1 m double monochromator, JOBON YVON U-1000[23]. In the TEM observation, a JEOL JEM-2010F with an acceleration voltage of 120 kV was used.

Fitting procedure

The spectrum was calculated by smearing out the density of states $D(E)$ with a gaussian curve ($2\sigma = 50$ meV) as the energy resolution function and with a lorentzian curve as the spectral lifetime broadening. In the calculation, Γ_d, Γ and E_S were taken as adjustable parameters, in which the deviation was adjusted by reference to $\Gamma_d = 0.13$ nm obtained in an optical measurement[24], and $\Gamma_d = 0.06$ nm obtained in X-ray diffraction measurement[32].

Received 20 May; accepted 22 September 2003; doi:10.1038/nature02074.

1. Voit, J. One-dimensional Fermi liquids. *Rep. Prog. Phys.* **57,** 977–1116 (1994).
2. Grioni, M. & Voit, J. in *Electronic Spectroscopies Applied to Low-dimensional Materials* (eds Hughes, H. P. & Starnberg, H. I.) 209–281 (Kluwer Academic, Dordrecht, 2000).
3. Mattsson, A. E., Eggert, S. & Johannesson, H. Properties of a Luttinger liquid with boundaries at finite temperature and size. *Phys. Rev. B* **56,** 15615–15628 (1997).
4. Egger, R. & Gogolin, A. O. Effective low-energy theory for correlated carbon nanotubes. *Phys. Rev. Lett.* **79,** 5082–5085 (1997).
5. Kane, C., Balents, L. & Fisher, M. P. A. Coulomb interactions and mesoscopic effects in carbon nanotubes. *Phys. Rev. Lett.* **79,** 5086–5089 (1997).
6. Egger, R. & Gogolin, A. O. Correlated transport and non-Fermi-liquid behavior in single-wall carbon nanotubes. *Eur. Phys. J. B* **3,** 281–300 (1998).
7. Bockrath, M. *et al.* Luttinger-liquid behaviour in carbon nanotubes. *Nature* **397,** 598–601 (1999).
8. Yao, Z., Postma, H. W. C., Balents, L. & Dekker, C. Carbon nanotube intramolecular junctions. *Nature* **402,** 273–276 (1999).
9. Postma, H. W. C., de Jonge, M., Yao, Z. & Dekker, C. Electrical transport through carbon nanotube junctions created by mechanical manipulation. *Phys. Rev. B* **62,** R10653–R10656 (2000).
10. Sonin, E. B. Tunneling into 1D and quasi-1D conductors: Luttinger-liquid behavior and effects of environment. *Physica E* **18,** 331–332 (2003).
11. Sekiyama, A. *et al.* Fermi-liquid versus Luttinger-liquid behavior and metal-insulator transition in N,N'-dicyanoquinonediimine-Cu salt studied by photoemission. *Phys. Rev. B* **51,** 13899–13902 (1995).
12. Gweon, G.-H. *et al.* Fermi surfaces and single-particle spectral functions of low-dimensional inorganic non-cuprate compounds: The molybdenum bronzes. *J. Phys. Condens. Matter* **8,** 9923–9938 (1996).
13. Zwick, F. *et al.* Band mapping and quasiparticle suppression in the one-dimensional organic conductor TTF-TCNQ. *Phys. Rev. Lett.* **81,** 2974–2977 (1998).
14. Denlinger, J. D. *et al.* Non-Fermi-liquid single particle line shape of the quasi-one-dimensional non-CDW metal $Li_{0.9}Mo_6O_{17}$: Comparison to the Luttinger liquid. *Phys. Rev. Lett.* **82,** 2540–2543 (1999).
15. Joynt, R. Pseudogaps and extrinsic losses in photoemission experiments on poorly conducting solids. *Science* **284,** 777–779 (1999).
16. Segovia, P., Purdie, D., Hengsberger, M. & Baer, Y. Observation of spin and charge collective modes in one-dimensional metallic chains. *Nature* **402,** 504–507 (1999).
17. Voit, J. *et al.* Electronic structure of solids with competing periodic potentials. *Science* **290,** 501–503 (2000).
18. Saito, R., Dresselhaus, G. & Dresselhaus, M. S. *Physical Properties of Carbon Nanotubes* (Imperial College Press, London, 1998).
19. Wildöer, J. W. G. *et al.* Electronic structure of atomically resolved carbon nanotubes. *Nature* **391,** 59–62 (1998).
20. Suzuki, S. *et al.* Electronic structure at carbon nanotube tips studied by photoemission spectroscopy. *Phys. Rev. B* **63,** 2454181–2454187 (2001).
21. Chen, P. *et al.* Electronic structure and optical limiting behavior of carbon nanotubes. *Phys. Rev. Lett.* **82,** 2548–2551 (1999).
22. Wakabayashi, T. *et al.* Towards the selective formation of specific isomers of fullerenes: T- and p-dependence of the yield of various isomers of fullerenes C_{60}-C_{84}. *Z. Phys. D* **40,** 414–417 (1997).
23. Kataura, H. *et al.* Optical properties of single-wall carbon nanotubes. *Synth. Met.* **103,** 2555–2558 (1999).
24. Ichida, M. *et al.* Exciton effects of optical transitions in single-wall carbon nanotubes. *J. Phys. Soc. Jpn* **68,** 3131–3133 (1999).
25. Yoshioka, H. Tomonaga-Luttinger-liquid behavior in conducting carbon nanotubes with open ends. *Physica E* **18,** 212–213 (2003).
26. Kwon, Y.-K., Saito, S. & Tomanek, D. Effect of intertube coupling on the electronic structure of carbon nanotube ropes. *Phys. Rev. B* **58,** 13314–13317 (1998).
27. Ouyang, M., Huang, J.-L., Cheung, C. L. & Lieber, C. M. Energy gaps in "metallic" single-walled carbon nanotubes. *Science* **292,** 702–705 (2001).
28. Maarouf, A. A., Kane, C. L. & Mele, E. J. Electronic structure of carbon nanotube ropes. *Phys. Rev. B* **61,** 11156–11165 (2000).
29. Odintsov, A. A. & Yoshioka, H. Universality of electron correlations in conducting carbon nanotubes. *Phys. Rev. B* **59,** R10457–R10460 (1999).
30. Liu, X. *et al.* Filling factors, structural, and electronic properties of C_{60} molecules in single-wall carbon nanotubes. *Phys. Rev. B* **65,** 0454191–0454196 (2002).
31. Vavro, J. *et al.* Electrical and thermal properties of C_{60}-filled single-wall carbon nanotubes. *Appl. Phys. Lett.* **80,** 1450–1452 (2002).
32. Abe, M. *et al.* Structural transformation from single-wall to double-wall carbon nanotube bundles. *Phys. Rev. B* 041405R (2003).

Acknowledgements We thank Y. Misaki for support with TEM observations. This study was performed with the approval of the Photon Factory Advisory Committee and under the Cooperative Research Program of HiSOR, Hiroshima Synchrotron Radiation Center, Hiroshima University. This study was supported in part by a Grant-in-Aid for Science Research from the Ministry of Education, Culture, Sports, Science and Technology of Japan.

Competing interests statement The authors declare that they have no competing financial interests.

Correspondence and requests for materials should be addressed to H.K. (kataura@phys.metro-u.ac.jp).

Migration of seismic scatterers associated with the 1993 Parkfield aseismic transient event

Fenglin Niu[1,2], Paul G. Silver[2], Robert M. Nadeau[3] & Thomas V. McEvilly[3]

[1]*Department of Earth Science, MS-126, Rice University, 6100 Main Street, Houston, Texas 77005, USA*
[2]*Department of Terrestrial Magnetism, Carnegie Institution of Washington, 5241 Broad Branch Road, NW, Washington DC 20015, USA*
[3]*Berkeley Seismological Laboratory, University of California Berkeley, and Earth Sciences Division, Lawrence Berkeley National Laboratory, Berkeley, California 94720, USA*

The time-varying deformation field within a fault zone, particularly at depths where earthquakes occur, is important for understanding fault behaviour and its relation to earthquake occurrence[1–3]. But detection of this temporal variation has been extremely difficult, although laboratory studies have long suggested that certain structural changes, such as the properties

of crustal fractures, should be seismically detectable[4]. Here we present evidence that such structural changes are indeed observable. In particular, we find a systematic temporal variation in the seismograms of repeat microearthquakes that occurred on the Parkfield segment of the San Andreas fault over the decade 1987–97. Our analysis reveals a change of the order of 10 m in the location of scatterers which plausibly lie within the fault zone at a depth of ~3 km. The motion of the scatterers is coincident, in space and time, with the onset of a well documented aseismic transient (deformation event). We speculate that this structural change is the result of a stress-induced redistribution of fluids in fluid-filled fractures caused by the transient event.

The Parkfield region of the San Andreas fault system is an ideal natural laboratory for studying structural changes in faults[5]. For more than a decade (1987–present), this region has been heavily instrumented, containing a variety of geodetic instruments as well as a network of ultrasensitive borehole seismometers. Of particular importance to the present study is the occurrence of a remarkable aseismic transient beginning in early 1993 (Fig. 1)[6–8] that represented a 30% increase in the slip rate along the San Andreas Fault. The transient was observed by essentially all types of available geodetic instruments, by temporal variations in seismicity rate as recorded by the borehole seismometers (the High Resolution Seismic Network, HRSN)[9], and was accompanied by the occurrence of four earthquakes of magnitude $M = 4+$ (that is, slightly more than four but less than five) from late 1992 to late 1994 (Fig. 1). The data suggest a complex aseismic/seismic episode, involving accelerated slip starting from the vicinity of the 1966 Parkfield earthquake, and migrating to the southeast, giving rise to geodetically observed surface slip[8]. It is, to our knowledge, the best-documented aseismic transient thus far observed.

This transient thus provides a well constrained environment to test for possible tectonically induced structural changes in the seismogenic crust. To perform this test, we have utilized tight clusters of repeating microearthquakes (magnitude $M \approx 1$) that have nearly the same location and mechanism. Recent dramatic improvements in the relative locations of small seismic events have revealed that a large fraction of seismicity occurs in these tight clusters[10,11]. The repeating events produce nearly identical seismograms when recorded at the same station, so that temporal changes in the medium can be more easily isolated from changes in the source. Clusters have been shown to be valuable in detecting post-seismic changes in the part of the seismogram known as S-wave coda, which represents scattered S-wave energy. For example, a study of the Loma Prieta earthquake of 1989 provided strong evidence, based primarily on travel times[12] and the decorrelation of the S-wave coda[13] that temporal variations in the wavefield could be observed from these events. Although promising, the interpretation of these post-seismic studies is complicated by the

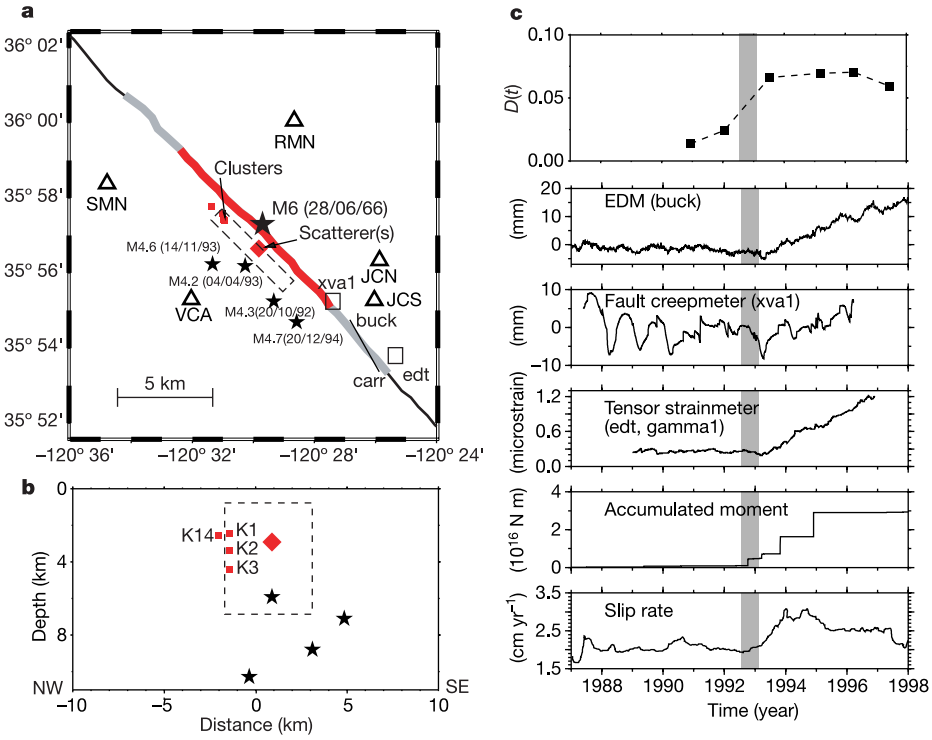

Figure 1 The Parkfield study area and geodetic results. **a**, Map view; **b**, cross-section; **c**, decorrelation index and geodetic recordings. **a**, **b**, The three-component borehole HRSN stations are shown as triangles. The red squares show the location of microearthquake clusters used in this study, denoted as K1, K2, K3 and K14. The black line shows the surface trace of the San Andreas fault. The thick grey line indicates the cross-section location shown in **b**. The large star is the epicentre of the 1966 $M = 6$ Parkfield earthquake, and the smaller stars denote the locations of the four $M = 4+$ events that occurred from 1992 to 1994. The dashed rectangle denotes the approximate location of the onset of the Parkfield aseismic transient in 1993, from recurrence intervals of event clusters[9]. The red section of fault denotes region of increased slip from inversion of geodetic data[8]. The locations of the EDM, creepmeter and strainmeter data shown in **c** are denoted by a black line and squares, respectively. **c**, Average temporal change in decorrelation index. $D(t)$, recorded by the HRSN stations from cluster K3 in this study (see Fig. 3 and text), along with representative geodetic recordings of the Parkfield aseismic transient (EDM measurements, creepmeter, tensor strainmeters), accumulated seismic moment release, and slip rate inferred from the repeat interval of clusters of events[10]. The grey bar denotes the roughly six-month time interval over which the observed change in seismic structure must have occurred, based on the analysis of all clusters.

possibility that the temporal variations are due to shallow coseismic crack formation and subsequent healing near the stations, and may be unrelated to post-seismic tectonic deformation[12]. In this study, we have made use of an aseismic transient to minimize the influence of coseismic crack formation. Also, the borehole HRSN has a greatly reduced environmental influence, compared to surface instruments, and thus provides an improved detection capability for subtle changes in the seismic wavefield, compared to previous studies.

We have examined a suite of candidate clusters that occurred near the $M = 6$, 1966 Parkfield earthquake (Fig. 1). The cluster with the greatest similarity between seismograms is referred to as K3, which is at 4 km depth; the events from this cluster produce virtually identical seismograms at a given station (Fig. 2a). Yet there are subtle differences in these records, and we seek to quantify these changes and then assess their cause. We have defined two parameters, the lag $\tau(t)$ and the decorrelation index $D(t)$ (see Methods), to quantify the difference between two seismograms. We found an obvious change that begins with the seismogram from the event occurring on 7 November 1993 (Fig. 2b, c). Of particular interest is the 'spike' of 4 ms in $\tau(t)$ about 2 s into the seismogram, which provides an important diagnostic for isolating the cause of this change. These waveform changes are clearly and systematically observed at all stations during the same time period (Fig. 3a).

We analysed a total of nine clusters located in nearly the same area as K3, so as to maintain a similar source–scatterer–receiver geometry. Among the nine clusters, we are able to confirm the observed change from the four clusters with the highest source similarity. The source similarity of a cluster is estimated by the average value, $\langle D \rangle$, of $D(t)$, for all pairs of seismograms in a cluster. Lower $\langle D \rangle$ corresponds to higher source similarity. The $\langle D \rangle$ values are 0.03–0.07 for the four clusters where the signal is observed, and 0.10–0.18 for the remaining five clusters. In each of the four clusters, the subtle change is relatively easy to identify from the two best stations, VCA and RMN (based on a comparison of station-specific source similarity). By combining the observations of different clusters, we can confine the time interval over which the medium change could have occurred to ~6 months (between 14 July 1992 and 5 February 1993; Fig. 1c).

A subtle but systematic difference in the waveforms in a cluster

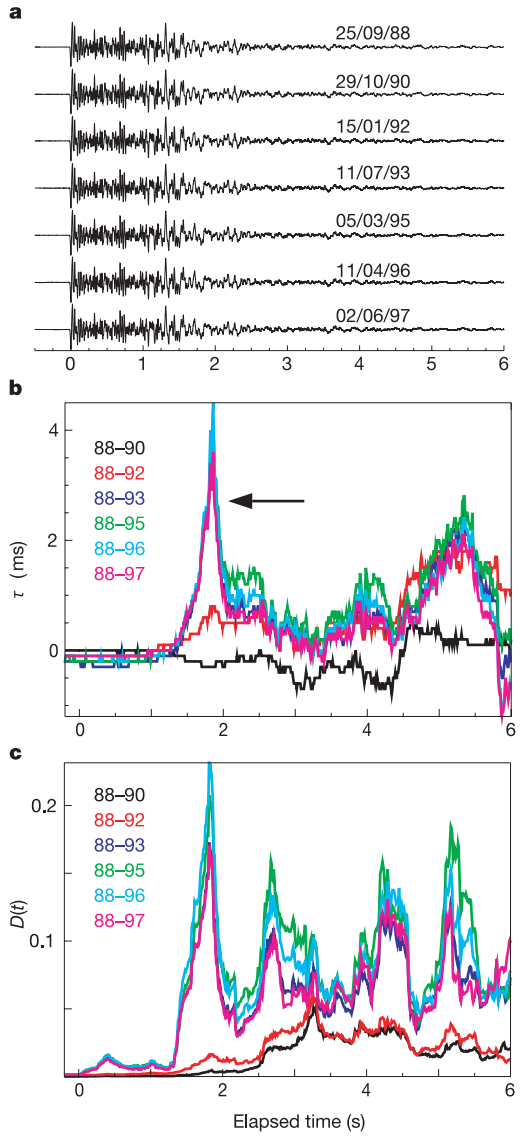

Figure 2 Cluster K3. Waveforms (**a**) and the calculated $\tau(t)$ (**b**) and $D(t)$ (**c**) of the components of cluster K3[17] recorded at station VCA. Data are aligned to the direct P wave. Note the high waveform similarity throughout the entire seismogram. Depth of the cluster is 4 km. To quantify the difference between seismograms, we compute the cross-correlation between the first seismogram (1988) and each subsequent seismogram within a 0.5-s moving time window. The lag time $\tau(t)$ is obtained when the maximum cross-correlation, $C_m(t)$, is reached, and a decorrelation index $D(t)$ is defined as $1 - C_m(t)$. Examples of $\tau(t)$ (**b**) and $D(t)$ (**c**) observed at station VCA. Note that there is a large spike in $\tau(t)$ at $t = 1.8$ s and large changes in $D(t)$, but only after 1993.

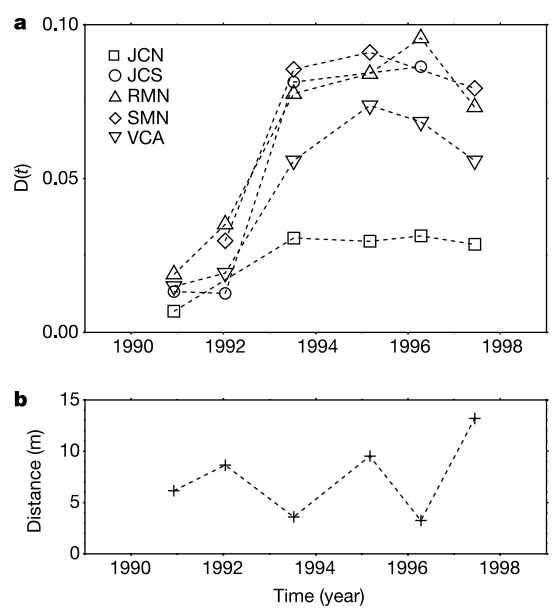

Figure 3 Temporal change in average $D(t)$ and relative distances of events with respect to the first event. **a**, Note the remarkable increase in $D(t)$ (averages calculated over 6 s of elapsed time) between 1992 and 1993 for all stations. The step-function increase in $D(t)$ suggests a temporal change in the medium at this time. **b**, Temporal changes of $\tau(t)$ and $D(t)$ could be due to systematic differences in earthquake location, if, for example, the pre- and post-1993 events are located in two separate subclusters. To test this, we measured the S–P travel times of each event–station pair and relocated all subsequent events relative to the first event. If the observed change in $D(t)$ is due to systematic variations in event location, these plots should have the same form as **a**. We see no such pattern, and conclude that the temporal variations in earthquake location did not produce the systematic variation in $D(t)$.

is most probably due to a change in the medium, or a slight difference of source parameters, or both. Numerical experiments, however, suggest that both background-velocity and earthquake-location models produce only long-period changes (Fig. 4) instead of the 'spike' variation shown in Fig. 2. On the other hand, a change in the location of a single scatterer results in a high-frequency and isolated 'spike' in $\tau(t)$ and $D(t)$ (Fig. 4). The same result could be caused by a localized reduction in velocity near the scatterer. The striking similarity between this synthetic and the lag time series in Fig. 2b and c for VCA strongly suggests that we are observing a change in the location of a single scatterer, or possibly a localized change in velocity in the vicinity of the scatterer.

In addition, if earthquake location were the cause of the systematic pattern in Figs 2 and 3a, the pre- and post-1993 events would have to be grouped into two separate subclusters. This is unlikely for two reasons. First, we measured the S–P times and relocated all subsequent events with respect to the initial event. If there were indeed two subclusters, then the distance from these events to the initial event should have the same form as Fig. 3a. In fact, the estimated distance pattern for K3 (Fig. 3b) shows no resemblance to the observed pattern in $D(t)$ (Fig. 3a). Second, such an explanation would require that all four clusters are coincidently composed of two subclusters: the pre- and post-1993 events. From these considerations we conclude that the observed temporal variation is not

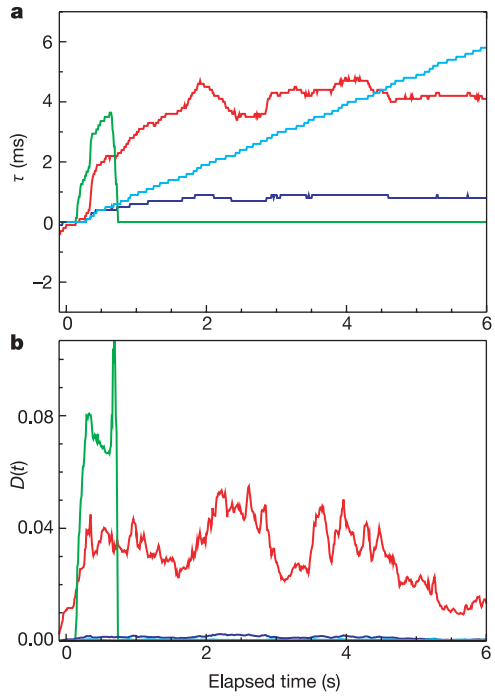

Figure 4 Quantities derived from synthetic seismograms **a**, $\tau(t)$; **b**, $D(t)$. Synthetics are calculated using an acoustic medium with a random distribution of scatterers, illustrating the effect of various temporal changes on these two functions: event location change of 2 m (blue) and 10 m (red), a decrease in background velocity of 0.1% (turquoise), and a 10-m change in the location of a single scatterer. All of these sources of change produce long-period variations, except a single scatterer, which produces a 'spike'. The observed spike (Fig. 2b) and other excursions are thus most easily explained by a change in the location of one, or only a few, scatterers. Although the acoustic synthetics is not strictly applicable to the problem of S waves, which requires a fully elastic treatment[18], it nevertheless fits our purpose of illustrating different effects due to changes in source and media rather than modelling the exact coda waveforms.

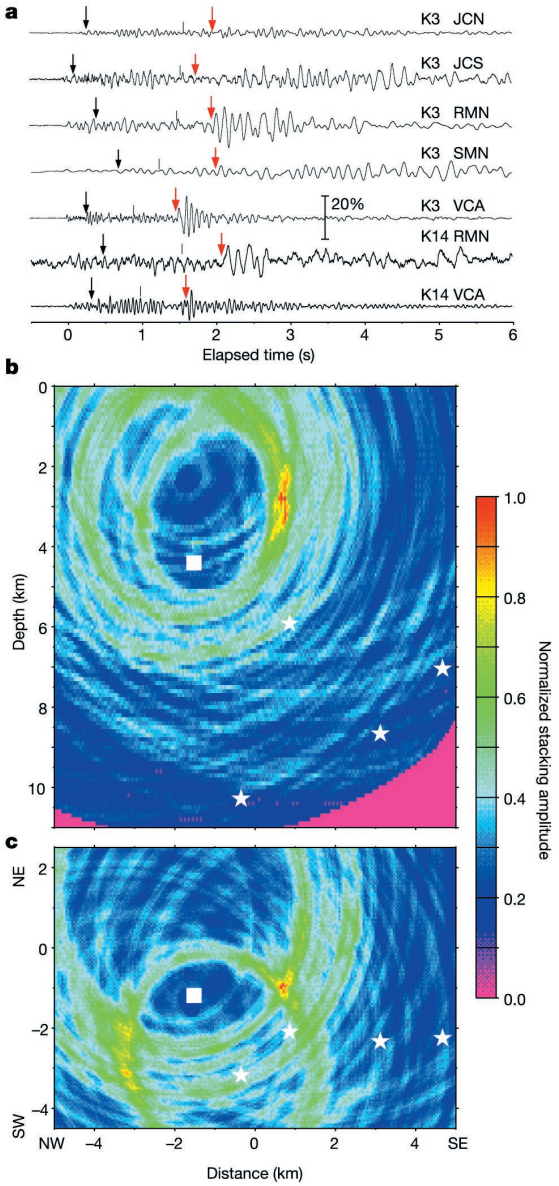

Figure 5 Differential vertical-component seismograms and the locations of the 'moving' scatterer(s). **a**, Differential vertical-component seismograms, $\delta s(t)$. Difference is taken between the average of post- and pre-1993 records. These seismograms enhance the parts of the seismogram that have changed in time. The records for VCA and RMN clearly show the contribution from a time-variable scatterer. Vertical bar denotes 20% of original P-wave amplitude. Note that for VCA, differential amplitude is comparable to overall coda amplitude in Fig. 2a. These seismograms were used to locate the time-variable scatterer by migration. Shown is the distribution of stacked amplitude, $A(\mathbf{x})$, as a function of position $\mathbf{x}$. It is normalized to the highest value. **b**, **c**, Cross-section parallel to the fault (**b**) and a map view at 3 km depth (**c**) that passes through the highest value of $A(\mathbf{x})$. The map reveals a well defined maximum (red spot) that is localized approximately 2 km southeast of the cluster along the San Andreas fault and at 3 km depth. Also shown is the location of cluster K3 (white square) and the locations of the four $M = 4+$ events that occurred between 1992 and 1994 (white stars). Note that the scatterer is closest to the event occurring on 4 April 1993. The medium change precedes this event. Predicted S-wave scatterer arrival times are shown by red arrows in (**a**). Also shown are the predicted direct-S arrival (vertical lines) and the predicted P-wave arrival times from the same scatterer (black arrows). Note that there is no comparable signal in the P-coda, consistent with the hypothesis that the scatterer is due to a fluid-filled fracture, which more efficiently reflects S than P.

due to differences in earthquake location, and is instead due to a change in the medium.

We have utilized a simple procedure for locating spatially the scatterers whose properties have changed in time, using differential seismograms (Fig. 5a) (see Methods). Stacking of differential seismograms clearly suggests a 'moving scatterer' located about 2 km to the southeast of the cluster (Fig. 5b) and at approximately 3 km depth (Fig. 5c). It corresponds to the 'spike' in lag time shown in Fig. 2b. Here we used a constant-velocity path model for each station such that the S-arrival times are fitted exactly. Such an approach approximately accounts for the three-dimensional structure where the direct-S and scattered-S paths are similar, and thus corrects for near-source structure as well as the particularly strong shallow heterogeneity beneath the receiver. There remains a possible error in scatterer location from three-dimensional structure that we estimate to be a few hundred metres, but which has essentially no effect on our scientific conclusions.

We also regard surface environmental effects, such as precipitation, to be an unlikely cause of the change in the medium. The largest effect related to precipitation will be an annual cycle, which would have little effect on the pattern in Fig. 3. Although 1993 did have increased precipitation compared to earlier years, the highest precipitation was in 1995, and this had no discernible effect on our data, as is clear from Fig. 3. Perhaps the strongest argument against an environmental explanation is that the depth of the resolved scatterer is large (3 km) and far removed from surface environmental effects.

From the high amplitude of the coda, we assume that the system is in the strong scattering regime, where the wavelength of the interacting wave is comparable to the size of the scatterer[14]. From this and the characteristic frequency of the seismic waves (10 Hz) we estimate the dimension of the scatterer to be of the order of 300 m. Assuming that scatterer migration is the cause of the time variation, we estimate a scatterer displacement of the order of 10 m from the 4-ms 'spike' (Fig. 2b; see Methods). Given the large magnitude of displacement, it is highly unlikely that this is the motion of a solid scatterer embedded within the medium; instead, it suggests that the scatterer is a fluid-filled fracture (or system of fractures) with the appropriate dimensions, containing fluid whose centroid has migrated 10 m. Such a fracture effectively represents a free-slip boundary and is a very efficient scatterer for shear waves polarized parallel to the plane of the fracture surface, although much less so for P waves. This may account for the absence of a comparable signal in the P-wave coda from this scatterer(s) (Fig. 5). If, alternatively, the observed change of waveform is caused by a velocity decrease near the scatterer (as mentioned above), it would most probably be due to a localized change in the density of fluid-filled cracks. Such a change would be equivalent to scatterer migration from a physical viewpoint, because both explanations appeal to fluid migration at or near the scatterer.

One possible explanation for this structural change is the coseismic deformation associated with the first of the four $M = 4+$ events (20 October 1992). In general, the primary influence of coseismic deformation is approximately within a single fault dimension, $\sim$1 km for an $M = 4+$ earthquake[15]. The scatterer is, however, about 6 km (six fault lengths) away from the 20 October 1992 earthquake, and probably too far to have a significant effect, although we cannot entirely exclude such a linkage. On the other hand, given the close correspondence (both spatially and temporally) between the change in the medium and the onset of the 1993 transient (Fig. 1), it is highly likely that this structural change was a further manifestation of the aseismic transient. Indeed, the inferred location of the scatterer essentially coincides with the zone of accelerated slip[9] that was active during the observed time of the scatterer change (Fig. 1). We thus speculate that the inferred fluid migration is either the direct result of the accelerated slip, or a more general response to the stress perturbation that gave rise to the transient event. □

Methods

Calculation of lag $\tau(t)$ and decorrelation index $D(t)$

To quantify the difference between seismograms in a cluster, we compute the cross-correlation between the first seismogram and each subsequent seismogram within a 0.5-s moving time window. The lag time $\tau(t)$ is obtained when the maximum cross-correlation, $C_m(t)$, is reached, and a decorrelation index $D(t)$ is defined as $1 - C_m(t)$. Both parameters constitute statistical measures of scatterer lag times. For a random distribution of scatterers and for characteristic frequency ω, $\tau(t)$ can be interpreted as the weighted mean $\langle\tau_i\rangle$ and $2D/\omega^2$ as the weighted variance σ_τ^2 (weighted by squared amplitude) of the time lags, τ_i, associated with the individual scatterers in the time window[16]. In relevant special cases, an actual time shift, t_s, can be retrieved from these statistics. For example, consider two populations of scatterers in a time window that are either shifted by t_s or unshifted. It can then be shown that $t_s = (\sigma_\tau^2 + \langle\tau_i\rangle^2)/\langle\tau_i\rangle$. For a single shifted scatterer in the time window, $t_s = \langle\tau_i\rangle$. In the more general case, $\langle\tau_i\rangle$ underestimates t_s. For our data, with a 20-Hz characteristic frequency, $\sigma_\tau \approx \langle\tau_i\rangle$, in which case we estimate the bias to be a factor of 2.

Locating 'moving' scatterers

To locate spatially the scatterer(s) whose properties have changed in time, we first constructed a differential seismogram $\delta s(t)$ by taking the difference of the average pre- and post-1993 seismograms for each station. For noise-free seismograms, $\delta s(t)$ will consist only of energy from any scatterer whose physical characteristics (location of scatterer, localized velocity change near the scatterer, or scatterer strength) have changed the amplitude or travel time of the scattered wave. Energy from an unchanged scatterer will be removed by this procedure. We then computed an nth-root ($n = 1$) summed amplitude, $A(\mathbf{x})$, of $\delta s(t)$ from each station, stacking on the predicted arrival time of a candidate scatterer originating from location $\mathbf{x}$. The location of the scatterer is determined as the maximum of the amplitude function, $A(\mathbf{x})$.

Received 1 November 2002; accepted 15 October 2003; doi:10.1038/nature02151.

1. Stein, R. S. The role of stress transfer in earthquake occurrence. *Nature* **402,** 605–609 (1999).
2. Freed, A. M. & Lin, J. Delayed triggering of the 1999 Hector Mine earthquake by viscoelastic stress transfer. *Nature* **411,** 180–183 (2001).
3. Bowman, D. D., Ouillon, G., Sammis, C. G., Sornette, A. & Sornette, D. An observational test of the critical earthquake concept. *J. Geophys. Res.* **103,** 24359–24372 (1998).
4. Nur, A. Effects of stress on velocity anisotropy in rocks with cracks. *J. Geophys. Res.* **76,** 2022–2034 (1971).
5. Bakun, W. H. & Lindh, A. G. The Parkfield, California, earthquake prediction experiment. *Science* **229,** 619–624 (1985).
6. Gwyther, R. L., Gladwin, M. T., Mee, M. & Hart, R. H. G. Anomalous shear strain at Parkfield during 1993-94. *Geophys. Res. Lett.* **23,** 2425–2428 (1996).
7. Langbein, J., Gwyther, R. L., Hart, R. H. G. & Gladwin, M. T. Slip-rate increase at Parkfield in 1993 detected by high-precision EDM and borehole tensor strainmeters. *Geophys. Res. Lett.* **26,** 2529–2532 (1999).
8. Gao, S. S., Silver, P. G. & Linde, A. T. Analysis of deformation data at Parkfield, California: Detection of a long-term strain transient. *J. Geophys. Res.* **105,** 2955–2968 (2000).
9. Nadeau, R. M. & McEvilly, T. V. Fault slip rates at depth from recurrence intervals of repeating microearthquakes. *Science* **285,** 718–721 (1999).
10. Nadeau, R. M., Antolik, M., Johnson, P. A., Foxall, W. & McEvilly, T. V. Seismological studies at Parkfield III: Microearthquake clusters in the study of fault-zone dynamics. *Bull. Seismol. Soc. Am.* **84,** 247–263 (1994).
11. Waldhauser, F. & Ellsworth, W. L. A double-difference earthquake location algorithm: method and application to the northern Hayward fault. *Bull. Seismol. Soc. Am.* **90,** 1353–1368 (2000).
12. Dodge, D. A. & Beroza, G. C. Source array analysis of coda waves near the 1989 Loma Prieta, California, mainshock: Implications for the mechanism of coseismic velocity changes. *J. Geophys. Res.* **102,** 24437–24458 (1997).
13. Baisch, S. & Bokelmann, G. H. Seismic waveform attributes before and after the Loma Prieta earthquake: Scattering change near the earthquake and temporal recovery. *J. Geophys. Res.* **106,** 16323–16337 (2001).
14. Aki, K. & Richards, P. G. *Quantitative Seismology: Theory and Methods* (Freeman, San Francisco, 1980).
15. Kanamori, H. & Anderson, D. L. Theoretical basis of some empirical relations in seismology. *Bull. Seismol. Soc. Am.* **65,** 1073–1095 (1975).
16. Snieder, R., Gret, A., Douma, H. & Scales, J. Coda wave interferometry for estimating nonlinear behavior in seismic velocity. *Science* **295,** 2253–2255 (2002).
17. Nadeau, R. M. & McEvilly, T. V. Seismological studies at Parkfield; V, Characteristic microearthquake sequences as fault-zone drilling targets. *Bull. Seismol. Soc. Am.* **87,** 1463–1472 (1997).
18. Poupinet, G., Ratdomopurbo, A. & Coutant, O. On the use of earthquake multiplets to study fractures and the temporal evolution of an active volcano. *Ann. Geofis.* **39,** 253–264 (1996).

Acknowledgements We thank the people who are involved in the installation and maintenance of the High Resolution Seismic Network, and also thank M. Fehler, P. Malin, E. Roeloffs, C. Thurber and L. Wen for discussions, and A. Rubin and S. Roecker for reviews. This work was supported by the Carnegie Institution of Washington, Rice University, NASA and USGS. Partial processing of the data was done at the University of California's Berkeley Seismological Laboratory and at the Center for Computational Seismology (CCS) at the Lawrence Berkeley National Laboratory.

Competing interests statement The authors declare that they have no competing financial interests.

Correspondence and requests for materials should be addressed to F.N. (niu@rice.edu.)